Inclusion of a Charge Sharing Correction Algorithm Into an X-Ray Photon Counting Spectral Detector Simulation Framework

O. L. P. Pickford Scienti , *Member, IEEE*, J. C. Bamber , *Member, IEEE*, and D. G. Darambara , *Member, IEEE*

Abstract—Most photon counting spectral imaging (x-CSI) simulations combine Monte Carlo techniques and experimental measurements to model signal output. These often omit some physical processes to minimize the computational resources needed, resulting in higher simulated energy resolutions compared with experiments. The aggregate effect of unsimulated processes can be compensated for using experimentally derived "blurring" factors. Blurring factors usually take the form of Gaussian convolutions of the simulation output to model system noise and collection inefficiencies. This approach is not suitable for applications involving charge sharing correction algorithm (CSCA) modeling, however, as most CSCAs operate in the prethresholding domain and across multiple pixels, incorporating variable amounts of noise and collection efficiency. To better model x-CSI CSCAs, this work introduces CoGI: a framework combining Monte Carlo and finite element methods to simulate photon-matter interaction, intrapixel charge transport, interpixel charge sharing, signal generation, and CSCA. CoGI is the first full x-CSI simulation framework to incorporate CSCA reported in the literature. CoGI has been validated in spectral and energy binning modes, using a γ-ray spectrometer and an Acteon series pixelated x-CSI detector, respectively. CoGI thus represents a versatile framework for comparing multiple ASIC-based CSCAs and will help inform future x-CSI system development.

Index Terms—Charge sharing correction, finite element method, hybrid pixelated detector, Monte Carlo, photon counting (PC), photon counting spectral imaging (x-CSI), spectral X-ray imaging.

I. INTRODUCTION

IN ORDER to realize good energy separation in medically focussed photon counting (PC) systems, materials with a high intrinsic energy resolution are required that can operate at medically relevant fluxes and with little additional cooling. Cadmium telluride (CdTe) and cadmium zinc telluride (CZT) are good candidate materials as they have higher absorption efficiencies at medically relevant energies than more commonly used semiconductor materials ($\sim$80% for 1-mm CdTe at 100 keV compared with $\sim$35% for Ge and $\sim$4% for Si) [1], as well as a relatively high charge carrier mobility and low pair production energy, leading to good energy resolution.

CdTe and CZT are thus fast becoming the standard choice for PC spectral imaging (x-CSI) applications.

Application-specific integrated circuits (ASICs) designed for PC spectral imaging typically utilize much smaller pixel sizes than conventional, energy integrating systems, with pixel pitches reaching down to 55 μm [2]. Smaller pixels are desirable as they allow for higher resolution images, however, in PC applications, they also assist in maintaining detector response at medically relevant fluxes. This is because, for a given X-ray flux, reducing the pixel size reduces the per pixel count rate, consequently reducing the necessary reset speed of the counting electronics. In imaging applications, the drive for ever smaller pixels is typically limited by two main factors: 1) reduced signal-to-noise ratios (SNR) and 2) increased chances of an incident photon's energy being spread across multiple pixels (charge sharing effects, CSE).

The decrease in SNR is caused by the reduction in true counts per pixel at smaller pixel sizes compared with electronic noise. PC systems can bypass this limitation by setting the trigger threshold such that it is above the electronic noise, meaning false counts due to electronic noise can be wholly excluded, and thus increasing SNR [3] even at lower pixel sizes. CSEs are more difficult to deal with, however, degrading both spatial and energy resolutions of PC systems. This is a significant limiting factor for pixel sizes in x-CSI systems [4], [5], as they rely on spectral information for material classification and quantification tasks [6]–[9].

It has been shown that by building charge sharing correction algorithms (CSCAs) into the ASICs, CSEs can be reduced and multiple imaging metrics effectively improved [10]. Such algorithms work by identifying events that occur in adjacent pixels within a short time window and using them to either determine the original photon's energy and location or else suppress these charge shared events. These algorithms have been shown to improve spectral response even for extremely small pixel sizes ($\sim$ 55 μm) [11], however, they usually come at some expense, e.g., reducing the flux, the ASIC can operate at before pileup becomes a problem [12] or identifying independent events as cases of charge sharing [13].

There are thus competing factors which combine to determine the optimal pixel size in an x-CSI system, which will vary depending on the CSCA employed, and currently no easy way to predict the optimal parameters *a priori*. Due to the high costs associated with x-CSI system prototyping, simulations may be used to optimize system parameters instead [14]–[16]. These simulations not only provide rapid prototype development (by comparing many systems without having to construct them) but also allow optimal parameters to be determined and for x-CSI to be compared with more mature imaging techniques such as dual energy CT [17]. To date, most full system simulations model the photon-detector interactions (e.g., by Monte Carlo approaches), use some kind of experimental data to determine simulation parameters (e.g., blurring [18] or equivalent voltage [19]), and then reconstruct signal based on a simulation of some or all of the electronics in the ASIC [20].

This work sets out to advance these simulations in three main ways.

1) By incorporating more physical processes of charge sharing than previous iterations of this simulation framework [21] such as photoelectron transport.
2) By including the signal induction contribution from clouds of holes moving in the sensor material.
3) By incorporating CSCAs at the ASIC level, allowing corrected energy resolutions to be simulated rather than intrinsic ones.

The resulting simulation framework will thus be able to model the widest range of system designs to date, allowing for the optimization of pixel dimensions for a given CSCA. Conversely, this framework can be used to solve the reverse problem and determine *in silico* the best CSCA for a given pixel dimension and spectral metric.

II. METHODS

A. Outline of Workflow

This work comprises four parts.

1) A detailed explanation of the simulation framework utilized and the physical processes modeled.
2) An experimental validation of the core physics behind the framework before the CSCA module is activated. This is done by comparing the simulated and experimental measurement for a commercially available γ-ray spectrometer with an ^{241}Am source, using energy resolution, spectral efficiency, and total photopeak detection efficiency as validation metrics.
3) A full simulation, including CSCA, to simulate the response of an XCounter Acteon series detector to a ^{57}Co source. The Acteon series detector is a pixelated, CdTe-based, PC detector and it is operated in the CSC mode in this work.

B. Simulation Framework

The simulation framework (referred to as CoGI) is nominally comprised of four "Processes." These processes combine to generate a 4-D matrix containing information on the time, intensity, and pixel location of every signal generated from the detector, allowing for the reconstruction of energy spectra or
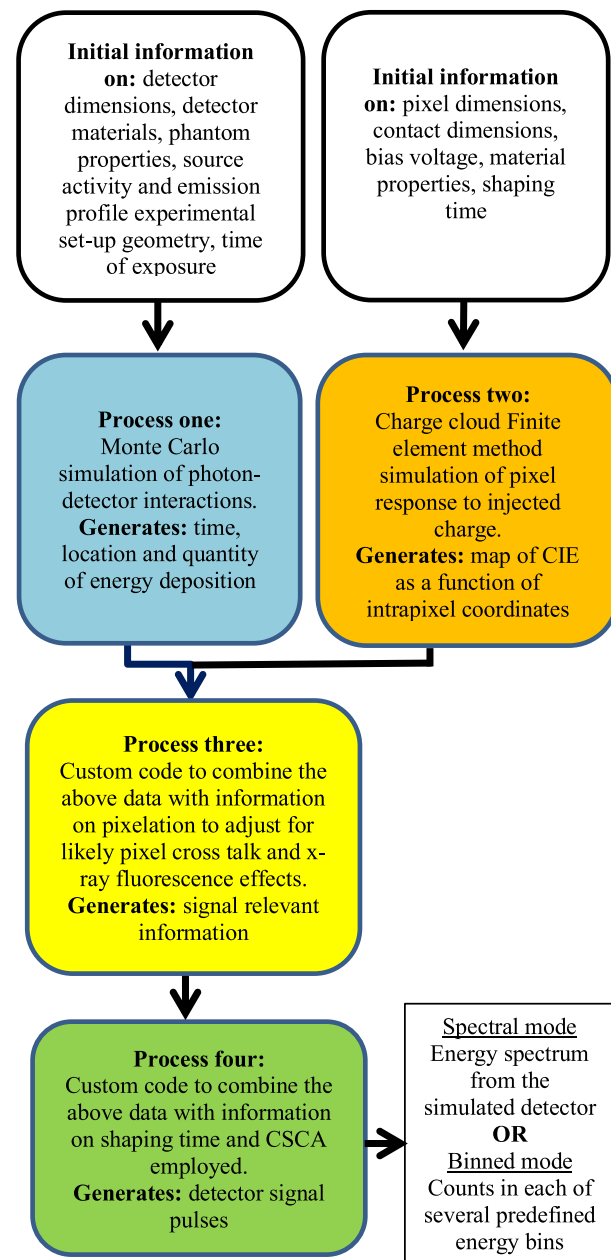

Fig. 1. Flowchart showing how information flows through CoGI. Information on the experimental setup, such as experiment geometry and material properties, are fed into process one, whilst information on the pixel configuration and electronics are fed into process two. The output from these two processes is then passed to process three, which combines the data and incorporates CSEs into the proto-signals file. This file is then passed to process four which applies CSCAs and gating time information to calculate the actual output signals. Further details on each module are given in the main body of the text.

energy binned images of the source to be produced. The layout of the framework can be seen in Fig. 1.

"Process one" is modeled using the open source "GATE" Monte Carlo code [20] and is where the material, shape, size, and relative geometry of the source, detector, and any relevant phantoms are defined. This code is used to model the processes of x/γ-ray emission, direct interactions with phantom/detector (elastic scattering, compton scattering, photoelectric absorption, and pair production), and mechanisms of secondary charge transport (X-ray flourescence, photoelectron escape,

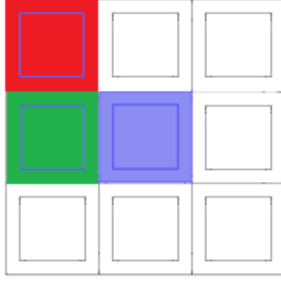| Parameter	Symbol	Value	Unit
Mobility, electrons	μ_e	1100	cm^2 V^{-1} s^{-1}
Mobility, holes	μ_h	100	cm^2 V^{-1} s^{-1}
Lifetime, electrons	τ_e	3.0	μs
Lifetime, holes	τ_h	2.0	μs
Density	P	5850	kg m^{-3}
Diffusion coefficient, electrons	D_e	2.84 x 10^{-3}	m^2 s^{-1}
Diffusion coefficient, holes	D_h	2.58 x 10^{-4}	m^2 s^{-1}
Relative permittivity	ε	11.0	-

Fig. 2. 3-D 3×3 grid of pixels used in calculating the CIE maps in COMSOL. Each pixel is defined as the central collecting anode (smaller squares) plus half of the distance between in and its neighboring anodes. Three pixel types were simulated in turn: "central" pixels surrounded by 8 others (purple, middle), "edge" pixels surrounded on all bar one side (green, left), and "corner" pixels surrounded on all bar 2 sides (red, top left).

and Auger electron production). Low energy events are simulated using Livermore low energy data. The output of this process is a list of individual interactions between the incident photons and the detector sensor material, which is passed directly to a custom MATLAB script ("Process three"). The passed list contains information on the spatial position, energy deposition, and time of each interaction.

Simultaneously, "Process two" models the process of charge collection in the detector pixels. To do this, information is needed on the pixel design (pixel size and shape, anode size and shape, and operating voltage) and sensor material properties (electron mobility, hole mobility, electron affinity, band gap, relative permittivity, and effective density of states in the valence and conduction bands). Values for the shaping time, operating voltage, and system geometry were obtained from the manufacturer under a nondisclosure agreement so cannot be disclosed here. Material properties modeled were averaged from literature values and are shown in Table I.

Three different types of pixel configuration are simulated: those surrounded on all sides by other pixels (center pixels), those with one exposed edge (edge pixels), and those with two exposed edges (corner pixels), as shown in Fig. 2. Note that a pixel (same colored region) is defined as the collecting anode plus half of the space between it and an adjacent electrode, as explained in Fig. 2. For each pixel configuration, a 3-D intensity map relating charge induction efficiency (CIE) to location within the pixel is generated. CIE is defined as

$$\text{CIE} = \frac{q}{Q} \tag{1}$$

where Q is the free charge produced in the detector by the ionizing interaction of an incident photon and q is the charge

induced at the collecting electrode due to the movement of these free charges. These CIE maps are determined by using the commercially available finite element method package COMSOL [22], to model the material's response to an applied electric field, as well as the processes of charge generation, drift, diffusion, and trapping. A time-dependent study is defined so that it solves the equation

$$\frac{\partial C}{\partial t} + \nabla \cdot (-D_c \nabla C) + U \cdot \nabla C = R \tag{2}$$

where C is the adjoint concentration of the charge carrier in question, D_C is the charge carrier's diffusion coefficient, U is the velocity field, and R is the reaction rate. By solving for times up to and including the shaping time of the preamplifier, a map can be generated which combines both the intrinsic CIE (based on charge transport) and the ballistic deficit (based on mismatch between shaping time and the time necessary for full charge collection). The value of D_C is material specific, and for our purposes we define U and R in the program as

$$U = -\mu_C \cdot \nabla \omega \tag{3}$$

and

$$R = \mu_C(\omega \cdot \omega_k) - \frac{C}{\tau_C} \tag{4}$$

where μ_C is the mobility of the charge carrier, τ_C is the average lifetime of free charge carriers, ω is the electric field in the pixel during operation, and ω_k is the weighting potential, defined as the electric field in the pixel when all contacts are set to 0 V except the collecting anode, which is set to 1 V. By substituting (3) and (4) into (2) we get

$$\frac{\partial C}{\partial t} + \nabla \cdot (-D_c \nabla C) \pm \mu_C \cdot \nabla \omega \cdot \nabla C = \mu_C(\omega \cdot \omega_k) - \frac{C}{\tau_C}. \tag{5}$$

Solving for the rate of change in charge gives

$$\frac{\partial C}{\partial t} = \mu_C \cdot \nabla \omega \cdot \nabla C + \nabla \cdot (D_c \nabla C) - \frac{C}{\tau_C} + \mu_C(\omega \cdot \omega_k). \tag{6}$$

This equation is comparable to Prettyman's adjoint continuity equation for determining the current induced in a collecting anode in a semiconductor detector [shown in (7)] [23], though note that Prettyman uses the symbols φ and φ_k in place of the symbols ω and ω_k, respectively

$$\frac{\partial C}{\partial t} = \mu_C \cdot \nabla \varphi \cdot \nabla C + \nabla \cdot (D_c \nabla C) - \frac{C}{\tau_C} + \mu_C(\nabla \varphi \cdot \nabla \varphi_k). \tag{7}$$

There is one obvious difference between (6) and (7): (6) contains the term $(\omega \cdot \omega_k)$ whereas (7) uses $(\nabla \varphi \cdot \nabla \varphi_k)$. To show why this has been done, we first expand the ∇ operators to give

$$\nabla \varphi \cdot \nabla \varphi_k = \left(\frac{\partial \varphi}{\partial x}\hat{x} + \frac{\partial \varphi}{\partial y}\hat{y} + \frac{\partial \varphi}{\partial z}\hat{z} \right)$$
$$\times \left(\frac{\partial \varphi_k}{\partial x}\hat{x} + \frac{\partial \varphi_k}{\partial y}\hat{y} + \frac{\partial \varphi_k}{\partial z}\hat{z} \right). \tag{8}$$

Next, we note that where the electric field is constant the electric potential will change linearly with distance from the anode. Close to the anode, the electric potential does not vary linearly, however, as the field is represented by a smoothly varying continuous function, it can be modeled as a series of linear segments, provided that the segments are sufficiently small. This criteria can be obtained by reducing the mesh size of the FEM such that the solution converged to does not change with further reduction in mesh size. In these small linear regions, we then have that

$$\varphi = ax + by + cz \tag{9}$$

and

$$\varphi_k = Fx + Gy + Hz \tag{10}$$

where a, b, c, F, G, and H are scalar constants. We thus find that

$$\nabla\varphi = \left(\frac{\partial(ax+by+cz)}{\partial x}\hat{x} + \frac{\partial(ax+by+cz)}{\partial y}\hat{y} + \frac{\partial(ax+by+cz)}{\partial z}\hat{z} \right) \tag{11}$$

and so

$$\nabla\varphi = a\hat{x} + b\hat{y} + c\hat{z}. \tag{12}$$

A similar argument can be made for φ_k which means that

$$\nabla\varphi \cdot \nabla\varphi_k = \left(a\hat{x} + b\hat{y} + c\hat{z}\right) \cdot \left(F\hat{x} + G\hat{y} + H\hat{z}\right) \\ = Fa + Gb + Hc. \tag{13}$$

Finally, we note that by defining ω and ω_k as vectors of the form

$$\omega = a\hat{x} + b\hat{y} + c\hat{z} \tag{14}$$

and

$$\omega_k = F\hat{x} + G\hat{y} + H\hat{z} \tag{15}$$

we get that

$$\omega . \omega_k = Fa + Gb + Hc \tag{16}$$

and thus the terms $\nabla\varphi \cdot \nabla\varphi_k$ and $\omega \cdot \omega_k$ give the same numerical answer. This complete FEM simulation thus produces a solution to Prettyman's adjoint continuity equations.

Examination of the terms in (6) shows that it models the charge carrier processes of generation ($\mu_C\omega \cdot \omega_k$), diffusion ($D_C\nabla C$), drift ($\mu_C\nabla\omega \cdot \nabla C$), and loss to trapping (C/τ_C), but that it does not include a term to account for the subsequent release of trapped charges. It should be noted, however, that due to the high voltage used across the pixels simulated, the residency time within the traps is sufficiently long compared to the drift time across the pixel that the effect of de-trapping on charge collection can be ignored to a first approximation.

The charge carriers modeled can be either electrons (e^-) or holes (h^+), however, the current COMSOL implementation can only deal with one at a time. In order to account for the signal contribution from both electrons and holes, the simulation is run separately for each pixel type: once with $C = e^-$ and once with $C = h^+$ (with the diffusion sign reversed). The

superposition of the resulting two CIE maps is used in CoGI to give a combined CIE map that considers both charge carriers in the detection process.

The output from Process two is thus a set of three files: one for each pixel configuration. These files contain the coordinates for an evenly spaced 3-D lattice within the pixel, and the corresponding charge induction efficiencies for those points for a given shaping time. CIE values between these grid points are determined as and when they are needed by trilinear interpolation of the nearest eight grid points.

Process three is executed in MATLAB and has the aim of combining information on CSEs from Process one (from X-ray fluorescence, photoelectron transport, and between pixel Compton scattering) and charge loss from Process two (due to interpixel diffusion, charge trapping, and ballistic deficit) into a single unified dataset. Data from the GATE simulation is pixelated using information from COMSOL and the events stored in a new file referred to as a "proto-signals file." During this transfer, X-rays that deposited their energy across multiple pixels are identified and separated into distinct events occurring in each affected pixel. For each event in the new file, the energy of the event is adjusted based on its relative position within its pixel, using information on CIE for the relevant pixel type produced in Process two. The output of Process three is then a 4-D matrix containing information on the proto-signal induced, time of interaction, and pixel coordinates (x and y) for each event.

"Process four" receives the proto-signals file and combines it with information on the user selected CSCA to simulate the results of the selected CSCA on the data. The CSCA used in this work is based on the proprietary AntiCoincidence algorithm employed in the XCounter Acteon detector being modeled [12]. Specifics of this particular CSCA are covered by a nondisclosure agreement, however, we can say that CSCAs in general operate by using a time window to identify events in adjacent pixels that likely result from charge sharing effects and then applying a corrective process to these events, either summing their energies together or excluding them entirely from the output. Finally, if operating in Binning mode, the user is prompted to set energy thresholds for the virtualized readout, in a similar way to any x-CSI system, so that reconstructed events can be assigned to the relevant energy bin. This allows for the simulated output to be compared to that measured by the readout of a physical x-CSI system.

C. Method for Validating the Basic Physics

In addition to the simulation of holes and CSCAs, the current incarnation of our simulation framework, now called CoGI, has had several upgrades to improve speed and robustness since our group last validated and published on it [14], [21]. In order to confirm that these changes have not affected the core physics of the simulation framework, we first revalidated the simulated output from CoGI in "Legacy" mode (without CSC algorithms) using a commercially available CZT-based γ-ray spectrometer (GR1 spectrometer, from Kromek [24]). This detector has only a single crystal pixel

and so does not suffer from pixelation-based CSEs or require CSC algorithms.

A 0.34 MBq ^{241}Am sealed source was placed in contact with, and approximately centered on, the spectrometer window and the energy spectrum produced over a 1-min exposure was recorded. A similar situation was then simulated in CoGI, with the main differences are as follows.

1) The Beryllium transmission window was omitted as the purity and thickness were unknown. We, therefore, expected our simulation to overestimate the number of photons detected below about ∼2 keV, as Beryllium windows are only partially transparent at these energies [25]. In order to avoid this contaminating our results, both the experimental and simulated data was assessed after removing any counts below 2.5 keV, so that only the energy regime in which Be windows are transparent were compared.

2) The coplanar electrode configuration was modeled as a simpler planar configuration, as we did not know the electrode specifications used to achieve a coplanar setup. We, therefore, accepted that our model would likely slightly underestimate energy resolution as a result of the increased contribution of holes to the signal in the simulation compared to our experiment.

The simulated and experimentally determined energy spectra were then compared in terms of their spectral efficiency (S_{eff}), total photopeak detection efficiency (T_{pp}), and the energy resolution at the photopeak. S_{eff} is defined as

$$S_{eff} = \frac{P_c}{T_c} \times 100\% \tag{17}$$

where P_c is the number of counts recorded in the photopeak and T_c is the total number of counts recorded in the detector. T_{pp} is defined as

$$T_{pp} = \frac{T_c}{\kappa} \times 100\% \tag{18}$$

where κ is the total number of photons emitted from the source during the acquisition time. In this work, the energy resolution of the photopeak is defined as the FWHM of a Gaussian fitted to the photopeak data.

D. Method for Validating CoGI's New CSCA Module

In order to experimentally validate the CSCA module of CoGI, a simulation was defined, using all modules, that modeled the detection of a ^{57}Co source by a physical system. The physical system used for this was an Acteon series pixelated detector (from XCounter [26]), with 256 × 128 pixels per ASIC and two energy thresholds per pixel. The total sensor area was 2.56 cm × 2.56 cm. In order to assess the efficacy of the CSCA during normal operation, the 2 available thresholds were set up such that an energy bin could be defined that would contain only the photopeak from the source. In order to ensure the correct placement of the thresholds, an energy spectrum of the source, as recorded by the Acteon detector, was required. Details of how this was acquired will be given later in this section. Once the energy spectrum was obtained, a Gaussian was fitted to the 122-keV photopeak and this modeled Gaussian
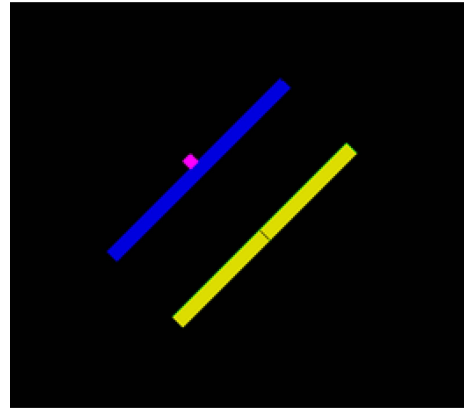

Fig. 3. Setup for simulation of ^{57}Co on the Acteon pixelated detector. The ^{57}Co source (small pink square) is placed in contact with the carbon fibre window (large blue rectangle) and directly over the gap between the two CdTe crystals (two smaller, yellow rectangles). The ASICs on which the CdTe crystals are mounted are not simulated, though the cathode and pixelated anodes are.

was used to define the energy bin for the simulation, such that the bin would contain ∼95% of the Gaussian area (peak energy ± 2σ). The physical detector output was then processed with the same two energy thresholds.

The detector used was based on a pixel pitch of 100 μm, a pixel thickness of 0.75 mm, and utilized CdTe as the X-ray conversion material. Full information was provided by the manufacturer with regards the material composition of the detector window, device geometries (internal and external), shaping times, CSC algorithm (AntiCoincidence), operating voltages, and ASICs configuration, allowing the corresponding simulation set-up to be as accurate as possible.

The experimental setup involved a ^{57}Co point source (1.12 MBq) placed directly onto the detector transmission window, approximately centered on the gap between two adjacent ASIC boards (aligned by hand during a scan in continuous acquisition mode). The CoGI simulation was set up to model the same physical situation, as shown in Fig. 3.

During the experimental setup, it was noticed that the calibration was slightly different on the two ASICs. Data was thus acquired and processed only from a single ASIC, and the simulation modified accordingly to reflect this. Data was acquired (experimentally and simulated) for 1 min of decay time and the number of counts in the defined energy bin was used as a metric for comparing the simulated CSCA effectiveness with the experimentally applied one.

E. Determination of Energy Thresholds for Photopeak Bin

In order to build up an energy spectrum of the source from only two thresholds, the lower-energy-threshold was held constant (to monitor consistency of the detector) whilst the upper-energy-threshold was moved in 1 keV steps between the lower threshold and 130 keV. One min of data was acquired for each 1-keV energy bin. The procedure for each 1-min acquisition was to:

1) normalize the number of counts in the lower-energy-bin to the counts recorded in the lower-energy-bin during the first 1-min acquisition;
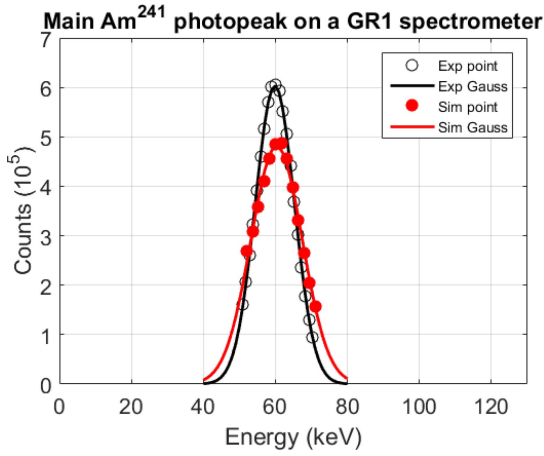
Fig. 4. Comparison of the main ^{241}Am photopeak as recorded by a GR1 spectrometer (Exp) and predicted by CoGI (Sim). The data recorded/simulated are shown (dots), along with the Gaussian fits (colored lines). The widths of the two peaks and areas underneath them are in good agreement.

2) scale the number of counts in the higher-energy-bin by the same number;
3) determine the number of counts in energy-bin j by calculating the number of counts above the high-energy-threshold when it was set to j keV, minus the counts above the high-energy-threshold when it was set to $(j + 1)$ keV.

The Gaussian fitted to the resulting 122-keV peak had a measured FWHM of 4.6 keV, in line with what would be expected based on information from the manufacturer ($\sim$4% at 120 keV). As the relation between FWHM and sigma for a Gaussian is

$$FWHM \approx 2.355\sigma \tag{19}$$

and for the Gaussian distributions $\sim$95% of the events occur in the interval mean $\pm 2\sigma$, we determined that the energy interval needed to capture $\sim$95% of the photopeak full energy counts was 118.1–125.9 keV. As the physical system was only capable of taking whole keV steps, the energy thresholds chosen for the validation work were 118 keV and 126 keV. The number of counts in this bin was thus given by the number of events above the 118 keV threshold minus the number of events above the 126 keV threshold. The simulated detector was calibrated based on the three prominent peaks in the spectrum before CSCA application and binning. These features were the Cd X-ray fluorescence, ^{57}Co full energy and escape peaks, as indicated in Fig. 5.

III. RESULTS

Fig. 4 shows the results from the experiments designed to validate the basic physics modeling in CoGI. Only the main photopeak for ^{241}Am decay (at around 60 keV) is shown here, as this is the dominant signal from this source. The measured points are shown for both the GR1 spectrometer (blue dots) and the CoGI simulation (red dots). As is routine in the γ-ray spectroscopy, Gaussians were determined (and plotted) for each dataset so that relevant metrics can be determined and compared, as shown in Table II.
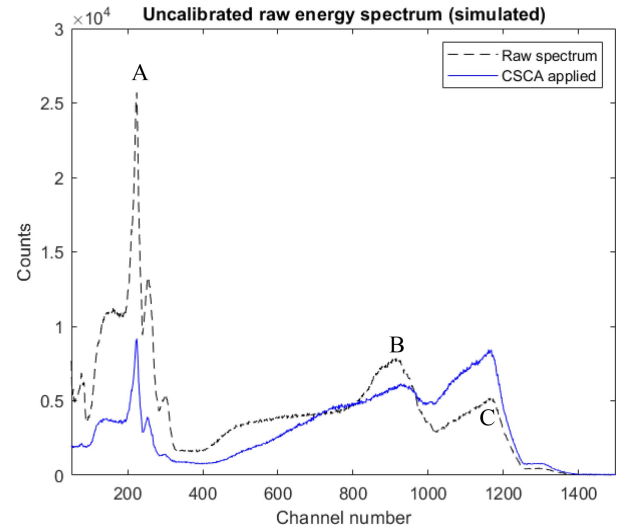

Fig. 5. Simulated ^{57}Co energy spectrum produced by CoGI with (solid blue line) and without (black dashed line) a CSCA applied. The spectral features corresponding to X-ray fluorescence (a), escape peak (b) and full-energy photopeak (c) from the raw spectrum were used to calibrate the simulated detector using a linear calibration technique.

TABLE II
COMPARISON OF PHOTOPEAK METRICS BETWEEN SIMULATION (CoGI) AND EXPERIMENT (GR1)

Metric	GR1	CoGI
FWHM (keV)	13	16
P_c	8.2E6	8.4E6
T_c	9.9E6	1.0E7
T_{PP} (%)	40.2	41.2
S_{eff} (%)	83	82

The energy resolution predicted by the simulation is poorer than that found experimentally, however, this was not unexpected considering the limitations on the simulation, and likely reasons for this are discussed in Sections II and IV. With these caveats noted, and based on the generally good agreement found for S_{PP}, P_c, T_c, and T_{PP}, the results were taken as validating the basic physics of the simulation framework, and so we moved on to consider the novel case where the CSCA is employed.

Fig. 5 shows the examples of the simulated ^{57}Co energy spectra measurements from CoGI, both before CSCA application (black dashed line) and after (solid blue line). In order to convert from simulated channel number to detected photon energy, a three point linear calibration was performed on the simulated detector using the spectral features of known energy: 1) the full energy photopeak (c); 2) escape peak (b); and 3) Cd $k\alpha$ line (a). If the applied voltage is sufficient to allow complete charge collection, from any pixel location, within the shaping time of the system then increasing the collection time should not shift the location of the main photopeak, as detrapping is not modeled and so lost charge cannot be collected, no matter how long is allowed for charge collection. Attempts at increasing collection time did cause a shift in photopeak location, however, indicating it is likely the shaping time modeled was inadequate for the combination of voltage and material properties modeled. Reasons for this and its implications are discussed further in Section IV. For now suffice it to say that,

TABLE III
COMPARISON OF COUNTS IN PHOTOPEAK CONTAINING ENERGY BIN
BETWEEN EXPERIMENT (ACTEON), SIMULATION (COGI) AND
SIMULATION WITH LONGER SHAPING TIME (COGI(LONG))

	Counts in photopeak bin	Discrepancy with experiment
Acteon (Physical)	3.11E5	N/A
CoGI	2.96E5	4.9%
CoGI (Long)	3.10E5	0.2%

in order to provide a better comparison with experiment, a second simulation was performed with a longer shaping time so that full pixel volume charge capture could be achieved. The output from this simulation with a longer shaping time did not require calibration, indicating that the shaping time was sufficient for charge to be fully collected from all pixel depths.

Table III shows the comparison between the number of counts in the energy bin for simulations and experiment. The counts presented are summed across all pixels in the array, and consequently contain contributions from center, edge, and corner pixel types.

IV. DISCUSSION

Table II shows that, when compared with a GR1 spectrometer, CoGI is able to accurately estimate the total photopeak detection efficiency (T_{PP} disagreement $\sim$2.4%) and gives a very good indication of the spectral efficiency to be expected (S_{eff} disagreement $\sim$1%). Whilst this is reassuring that the physics relevant to a nonpixelated detector are correctly modeled, it should be noted that CoGI does underestimate the energy resolution by a full $\sim$3 keV. This disparity between the experimentally determined FWHM and that predicted by the simulations is due to a limitation of the simulation setup, specifically the electrode configuration. As noted in Section II, the GR1 uses a coplanar electrode arrangement whilst CoGI was setup to model a planar setup. CoGI could not model the coplanar arrangement in this case because information on the geometry and voltages of the GR1's coplanar configuration of electrodes was not available. Coplanar arrangements are designed to screen out signal contribution from holes, which have lower mobility and are more readily trapped, leading to a more severe degradation in energy resolution. Consequently, it would be expected that the simulation results of a planar arrangement would overestimate the FWHM compared to a coplanar arrangement, as was found.

The data from Table II thus validates that the basic physics of our simulation framework are intact and we can proceed with deploying it to the new situation of a pixelated detector operating a CSCA.

Fig. 5 shows simulated ^{57}Co spectra from CoGI, as recorded by a simulated version of the Acteon detector, both with and without a CSCA employed. It can be seen that the CSCA modeled (based on XCounter's proprietary AntiCoincidence mode) produces a clear reduction in the X-ray fluorescence peaks (a), as well as a marked increase in the ratio between the full energy and escape peaks (c and b, respectively). As the sensor is being exposed to mono-energetic photons, and so only a single photopeak would be expected without charge sharing, this

clearly demonstrates that the algorithm is able to identify instances in which charge was shared across multiple pixels and recombine these counts from different pixels into a single peak of corrected energy.

The maps used in calculating the output signal include signal loss from charge trapping, charge diffusion to adjacent pixels and ballistic deficit.

Ballistic deficit is a loss in signal output resulting from a shaping time which is too short to allow charge clouds to drift fully to the anode during collection time, regardless of their depth within the pixel. We refer to the situation where shaping time is long enough to minimize ballistic deficit as full pixel volume charge collection (FPVCC). Once FPVCC is reached, further increasing the shaping time should not result in a shift in the output signal (channel number of the photopeak). Sequential variation of the simulated shaping time in our setup did result in an increase in the photopeak channel number up to a maximum of 1220, where it stabilized. Combining this data with that in Fig. 5, it becomes clear that whilst the physical system possessed a sufficiently long shaping time for FPVCC to be realized, the simulated system did not. When the physical system's parameters were modeled the photopeak was shifted down to channel $\sim$1770, indicating ballistic deficit. This strongly suggests that the combination of applied voltage and shaping time simulated for this material do not allow for FPVCC to occur. The electronics properties used in our simulations were provided by the manufacturer, and further discussions with them led us to believe that the physical system had been shown to demonstrate FPVCC. The most likely reason for the lack of FPVCC from our simulation, therefore, seems to be the use of averaged literature values for some of the material parameters, as different material properties would result in different shaping times needed to achieve FPVCC. The FPVCC condition could, however, be artificially produced by extending shaping time. As detrapping is not simulated in this framework, such longer shaping times would reduce ballistic deficit without impacting on the proportion of charge lost to trapping, and so seemed a reasonable approach to take. We, therefore, proceeded to continue the analysis with two simulations in CoGI.

1) Manufacturer provided voltages and shaping times with literature averaged material properties. This simulated detector required three-point linear calibration to correct for ballistic deficit.
2) Manufacturer provided voltage and literature averaged material properties but a longer shaping time so that FPVCC was achieved. This detector did not require calibration as all spectral features were found in the expected energy bins.

The energy thresholds set on the physical system were then replicated in the simulation, and the number of counts in the photopeak bin recorded for all three setups, as shown in Table III. As can be seen from this setup, good agreement ($<$5% deviation) is found between the outputs of a physical and CoGI simulated Acteon system, even when the CdTe material properties are averaged from literature values rather than based on the exact CdTe formulation used and FPVCC is not achieved. Extension of shaping time to replicate the FPVCC state found in the physical system further

improves the agreement between simulation and reality, with the discrepancy reduced to ∼0.2%.

Collectively, these results provide strong evidence validating CoGI as a simulation framework capable of modeling X-ray PC spectral detectors, including cases where CSCAs are employed.

V. CONCLUSION

This work has involved a two-part validation of the simulation framework referred to as CoGI. The basic physics of the simulation in a nonpixelated, noncharge sharing situation were validated using a commercially available GR1 γ-ray spectrometer, whilst the pixelated, charge sharing correction case was validated using an Acteon series PC detector from XCounter, running in their proprietary AntiCoincidence mode.

It was demonstrated that the CoGI simulation framework can predict the output of a defined energy bin in the Acteon detector with good accuracy (<5% deviation from experiment) when provided with pixelation dimensions, operating voltages, a CSCA, shaping times, and material properties. Importantly, this work was able to model system outputs accurately using very small pixel pitches (100 μm), a regime in which CSEs can be significant. Further, CoGI was shown to be accurate (∼0.2% deviation from experiment) even when exact material properties were not known, provided that the physical system's design allows charge clouds to fully drift to the anode within the shaping time, regardless of their point of creation within the pixel: a condition referred to as FPVCC. This was possible by using an artificially long shaping time for signal collection such that FPVCC was achieved in the simulation. The ability to use averaged material properties like this allows for a wider range of systems to be simulated, as material properties do not need to be extensively characterized for each one.

Inclusion of an ASIC-based CSCA directly into the signal reconstruction makes CoGI an especially useful model for determining the response of small pixel systems (<200 μm) in spectral applications, such as x-CSI, where CSCAs are used to preserve spectral response. Whilst XCounter's AntiCoincidence algorithm was modeled in this case and shown to be useful in reducing charge sharing artifacts even at these small pixel sizes, CoGI could be easily adapted to model any ASIC-based CSCA. Optimization of pixel parameters can thus be performed based on the corrected signal they produce rather than the initial signals they induce. The realism of this simulation framework is expected to be of great interest to those developing both physical systems and those working on truly spectral reconstruction algorithms, by giving them access to realistic image data without requiring the expensive investment in the prototype x-CSI systems. The next iteration of CoGI will aim to further facilitate these works by providing some basic material decomposition algorithms to allow for application specific questions to be answered.

REFERENCES

[1] T. Takahashi and S. Watanabe, "Recent progress in CdTe and CdZnTe detectors," *IEEE Trans. Nucl. Sci.*, vol. 48, no. 4, pp. 950–959, Aug. 2001.

[2] R. Ballabriga, M. Campbell, and X. Llopart, "Asic developments for radiation imaging applications: The medipix and timepix family," *Nucl. Instrum. Methods Phys. Res. A, Accelerators Spectrometers Detectors Assoc. Equip.*, vol. 878, pp. 10–23, Jan. 2018.

[3] P. Shikhaliev, "Computed tomography with energy-resolved detection: A feasibility study," *Phys. Med. Biol.*, vol. 53, no. 5, pp. 1475–1495, 2008.

[4] K. Taguchi and J. S. Iwanczyk, "Vision 20/20: Single photon counting X-ray detectors in medical imaging," *Med. Phys.*, vol. 40, no. 10, 2013, Art. no. 100901, doi: 10.1118/1.4820371.

[5] R. Ballabriga *et al.*, "Photon counting detectors for X-ray imaging with emphasis on CT," *IEEE Trans. Radiat. Plasma Med. Sci.*, early access, Jun. 16, 2020, doi: 10.1109/TRPMS.2020.3002949.

[6] E. Roessl and R. Proksa, "K-edge imaging in X-ray computed tomography using multi-bin photon counting detectors," *Phys. Med. Biol.*, vol. 52, pp. 4679–4696, Aug. 2007.

[7] R. Aamir *et al.*, "MARS spectral molecular imaging of lamb tissue: Data collection and image analysis," *J. Instrum.*, vol. 9, Feb. 2014, Art. no. P02005.

[8] X. Wang, K. Taguchi, D. Wagenaar, B. Patt, and E. Frey, "Material separation in X-ray CT with energy resolved photon-counting detectors," *Med. Phys.*, vol. 38, no. 3, pp. 1534–1546, 2011.

[9] Y. Lu *et al.*, "Material decomposition using ensemble learning for spectral X-ray imaging," *IEEE Trans. Radiat. Plasma Med. Sci.*, vol. 2, no. 3, pp. 194–204, May 2018.

[10] T. Koenig *et al.*, "How spectroscopic X-ray imaging benefits from inter-pixel communication," *Phys. Med. Biol.*, vol. 59, pp. 6195–6213, Sep. 2014.

[11] T. Koenig *et al.*, "Charge summing in spectroscopic X-ray detectors with high-Z sensors," *IEEE Trans. Nucl. Sci.*, vol. 60, no. 6, pp. 4713–4718, Dec. 2013.

[12] C. Ullberg, M. Urech, C. Eriksson, A. Stewart, and N. Weber, "Photon couting dual energy x-ray imaging at CT count rates: Measurements and implications of in-pixel charge sharing correction," in *Proc. SPIE Med. Imag.*, vol. 10573, 2018, Art. no. 1057319.

[13] M. Veale *et al.*, "Measurements of charge sharing in small pixel CdTe detectors," *Nucl. Instrum. Methods Phys. Res. A, Accelerators Spectrometers Detectors Assoc. Equip.*, vol. 767, pp. 218–226, Dec. 2014.

[14] P. Guerra, A. Santos, and D. G. Darambara, "An investigation of performance characteristics of a pixellated room-temperature semiconductor detector for medical imaging," *J. Phys. D, Appl. Phys.*, vol. 42, no. 17, 2009, Art. no. 175101.

[15] P. Guerra, A. Santos, and D. G. Darambara, "Development of a simplified simulation model for performance characterization of a pixellated CdZnTe multimodality imaging system," *Phys. Med. Biol.*, vol. 53, pp. 1099–1113, Feb. 2008.

[16] M. Myronakis and D. G. Darambara, "Monte Carlo investigation of charge-transport effects on energy resolution and detection efficiency of pixelated CZT detectors for SPECT/PET applications," *Med. Phys.*, vol. 38, pp. 455–467, Jan. 2011.

[17] M. Yveborg, M. Danielsson, and H. Bornefalk, "Theoretical comparison of a dual energy system and photon counting silicon detector used for material quantification in spectral CT," *IEEE Trans. Med. Imag.*, vol. 34, no. 3, pp. 796–806, Mar. 2015.

[18] E. Roessl, B. Brendel, K.-J. Engel, J. Schlomka, A. Thran, and R. Proksa, "Sensitivity of photon-counting based K-edge imaging in X-ray computed tomography," *IEEE Trans. Med. Imag.*, vol. 30, no. 9, pp. 1678–1690, Sep. 2011.

[19] P. Trueb, P. Zambon, and Z. Bronnimann, "Assessment of the spectral performance of hybrid photon counting X-ray detectors," *Med. Phys.*, vol. 44, no. 9, pp. e207–e214, 2017.

[20] S. Jan *et al.*, "GATE: A simulation toolkit for PET and SPECT," *Phys. Med. Biol.*, vol. 49, pp. 4543–4561, Sep. 2004.

[21] M. Myronakis, M. Zvelebil, and D. Darambara, "Computational modelling of pixelated CdZnTe detectors for X- and γ-ray imaging applications," *J. Instrum.*, vol. 7, no. 3, 2012, Art. no. P03004.

[22] *COMSOL Multiphysics®v5.2a*. Accessed: Feb. 12, 2020. [Online]. Available: www.comsol.com

[23] T. Prettyman, "Method for mapping charge pulses in semiconductor radiation detectors," *Nucl. Instrum. Methods Phys. Res. A, Accelerators Spectrometers Detectors Assoc. Equip.*, vol. 422, nos. 1–3, pp. 232–237, 1999.

[24] *Kromek GR1 γ-spectrometer*. Accessed: Feb. 12, 2020. [Online]. Available: https://www.kromek.com

[25] Y. Liao. (2018). *Practical Electron Microscopy and Database*. [Online]. Available: www.globalsino.com/EM/

[26] *XCounter Acteon Detector*. Accessed: Feb. 12, 2020. [Online]. Available: https://directconversion.com/product/xc-actaeon/